IMPACT OF GRATING DUTY-CYCLE RANDOMNESS ON DFB LASER PERFORMANCE

IMPACT OF GRATING DUTY-CYCLE RANDOMNESS ON DFB LASER PERFORMANCE

By MANPO YANG, B. ENG.

A Thesis Submitted to the School of Graduate Studies in Partial Fulfilment of the Requirements for the Degree Master of Applied Science

McMaster University MASTER OF APPLIED SCIENCE (2024) Hamilton, Ontario

TITLE: Impact Of Grating Duty-Cycle Randomness on DFB Laser Performance

AUTHER: Manpo Yang

B.ENG. (Beijing University of Technology, Beijing, China)

SUPERVISOR: Dr. Xun Li

Professor, Department of Electrical and Computer Engineering

NUMBER OF PAGES: viii, 56

Abstract

The duty-cycle randomness (DCR) lying the Bragg grating of the distributed feedback (DFB) lasers introduced by the fabrication process is inevitable even with the state-of-the-art technologies such as the electron beam lithography and dry or wet etching. This thesis investigates the impact of grating DCR on DFB laser performance through numerical simulations. The result reveals that such a randomness causes a reduction on the side mode suppression ratio (SMSR), and deteriorates the noise characteristics, i.e., broadens the linewidth and increases the relative intensity noise (RIN). With the grating DCR, the effective grating coupling coefficient decreases as evidenced by the reduced Bragg stopband width. However, the longitudinal spatial hole burning (LSHB) effect in the DFB lasers can somewhat be diminished by the grating DCR. The seriousness of these effects depends on different grating structures and their coupling strengths. Our simulation shows that a degradation of 17dB can be brought to the SMSR of the uniform grating DFB lasers with their duty-cycles taking a deviation of $\pm$25% in a uniformly distributed random fashion. It also broadens the linewidth of the quarter-wavelength phase-shifted DFB lasers by more than 2.5 folds. The impact of this effect on the RIN is moderate – less than 2%. All the performance deteriorations can partially be attributed to the effective reduction of the grating coupling coefficient around 20% by such a DCR.

Acknowledgements

I would like to take this opportunity to thank all those who have made the completion of this thesis possible. I would like to express my sincerest appreciation to my supervisor, Dr. Xun Li for his help in my research. His guidance, encouragement and keen insights are highly appreciated and will always be remembered. The knowledge acquired from Dr. Li is indispensable and will be tremendously beneficial in my future career.

Furthermore, I wish to thank Ms. Cheryl Gies for the administrative assistance, and my colleagues Dr. Chuanning Niu, Mr. Xiangpeng Kong. Their help and friendship have made this an experience to remember and cherish.

Finally, I would like to express my grateful thanks to my father and my mother. Thank you for your unconditional love and support.

Abbreviations

AR: augmented reality

CPM: corrugation-pitch modulation

DCR: duty-cycle randomness

DBR: distributed Bragg reflector

DFB: distributed-feedback

EPON: Ethernet Passive Optical Network

FP: Fabry-Perot

FTTH: Fiber to the Home

GPON: Gigabit Passive Optical Network

LD: laser diode

LI: light power vs current

LSHB: longitudinal spatial hole burning

PON: Passive Optical Network

RIN: relative intensity noise

SMSR: side-mode suppression ratio

SWM: standing wave method

TD: time domain

TMM: transfer matrix method

TWM: travelling wave method

VCSEL: vertical cavity surface emitting laser

VR: virtual reality

1D: one-dimensional

Contents

List of Figures

Chapter 1

Introduction

1.1 Overview of Optical Communications and the Development of Semiconductor Lasers

Optical fiber communication, which utilizes light waves as the carrier for information and optical fibers as the medium of transmission, represents a pivotal mode of communication. This method is increasingly gaining prominence within the field of communications, attributed to its vast communication capacity and minimal transmission losses. Beyond these merits, optical fiber communication also boasts resistance to electromagnetic interference and enhanced security features, further solidifying its advantageous position.

Since the advent of semiconductor lasers, they have been recognized as exceptionally suited for serving as the light source in optical fiber communications. Despite their low power output, semiconductor lasers boast high photoelectric conversion efficiency, low threshold, and small driving currents, while optical fiber communication does not necessitate high laser power. Moreover, the compact size of semiconductor lasers and the wavelength of

emission, which depends on the semiconductor material of the active region, can be precisely tuned to fall near 1310 nm and 1550 nm through an appropriate selection of materials and compositional ratios, aligning perfectly with the transmission windows of optical fiber communications [1]. These characteristics enable a highly effective integration with optical fibers, leading to their widespread application in the field of optical communications. Consequently, since their introduction, semiconductor lasers have received considerable attention and have rapidly advanced. Indeed, the emergence of semiconductor lasers has significantly propelled optical fiber communication toward practical application.

The development of optical fiber communication dates back to the 1960s. As early as 1966, the concept of optical fiber communication and the theory of dielectric waveguides were proposed by the British-Chinese scientist Charles K. Kao, who also predicted that long-distance fiber optic communication would become feasible if the impurities in glass fiber waveguides could be significantly reduced, leading to the creation of low-loss optical fibers [2]. However, due to the high transmission losses in optical fibers at that time, it was not until 1970, when Corning Incorporated developed fibers with lower losses, that optical fiber communication began to attract attention, spurring research into light sources for fiber communications. In the same year, the continuous-wave operation of a room-temperature double heterostructure semiconductor laser was developed [3,4], providing a stable and reliable light source for optical fiber communication. Thereafter, the development of optical fibers and light sources complemented each other, and both made significant progress in

the subsequent years. In 1972, Corning started producing low-loss optical fibers with 2 dB/km loss. By 1974, Bell Labs had successfully developed optical fibers with a loss as low as 1 dB/km. In 1976, Japan developed optical fibers with a wavelength of 1.3 μm and a transmission loss of 0.5 dB/km. In 1978, long-wavelength optical fibers with a wavelength of 1.55 μm and a loss as low as 0.2 dB/km were successfully developed. Currently, the loss in optical fibers can be reduced to less than 0.16 dB/km. Meanwhile, short-wavelength semiconductor lasers have been developed to a practical level. Bell Labs and the Japanese Telegraph and Telephone Corporation (NTT) developed room-temperature continuous-operation semiconductor lasers with lifespans exceeding 100,000 hours and wavelengths of 0.8 μm to 0.9 μm, rapidly commercializing the light source for the first optical communication window. The United States and Japan, among other countries, subsequently conducted optical fiber system transmission experiments. In 1975, the MIT Lincoln Laboratory first developed InGaAsP double heterostructure lasers in the 1.2 μm to 1.3 μm band [5], thereby obtaining the light source for the second communication window. That same year, Bell Labs conducted the first point-to-point optical fiber communication system experiment. Japan accelerated its research on semiconductor lasers, quickly developing long-wavelength lasers in the 1.5 μm to 1.6 μm range, leading to the emergence of the light source for the third optical communication window. In 1981, Laser Diode Electronics Inc. in the United States began selling a type of semiconductor laser with a wavelength of 1.5 μm, the QL5-1500 model. In the following years, an increasing number of optical cables and fiber links were laid and established.

This observation highlights that optical fibers and semiconductor lasers, as the two main pillars of optical communication, have been continuously advancing in tandem. From the perspective of technological development, it appears that optical fibers have progressed more rapidly, while semiconductor lasers have evolved more gradually. Over the past several decades, semiconductor lasers have consistently kept pace with the advancements in optical fibers, making strides in mode structure, reliability, operational lifespan, and wavelength diversity.

Today, with the rapid development of mobile communications, big data, and cloud computing, data services are experiencing explosive growth, and the global communications industry is on the cusp of a new wave of transformation. With the rise and growth of applications like 4K video, augmented reality (AR), and virtual reality (VR), there is an increasing demand for network bandwidth, especially for fixed network bandwidth access from users. In response to the escalating demand for service bandwidth, the trend of upgrading optical fiber to the home (FTTH) network construction from EPON and GPON technologies to 10G PON has become inevitable. Furthermore, in recent years, there has been a surge in the deployment of 100G Ethernet optical transceivers in data centers. According to the latest report from the market research firm LightCounting, large data center operators began to deploy 100G Ethernet optical transceivers on a large scale starting in the first half of 2016. LightCounting states that the data centers' insatiable demand for 100GbE optical transceivers has led to a shortage of high-end optical components such as distributed feedback laser diodes.

1.2 Common Semiconductor Lasers in Optical Fiber Communication Systems

1.2.1 Fabry-Perot Laser Diode

The F-P LD (Fabry-Perot laser diode) is currently the simplest in structure and the easiest to implement among semiconductor lasers. It is a type of semiconductor laser that uses a Fabry-Perot (FP) cavity as its resonant chamber to emit multi-longitudinal mode coherent light.

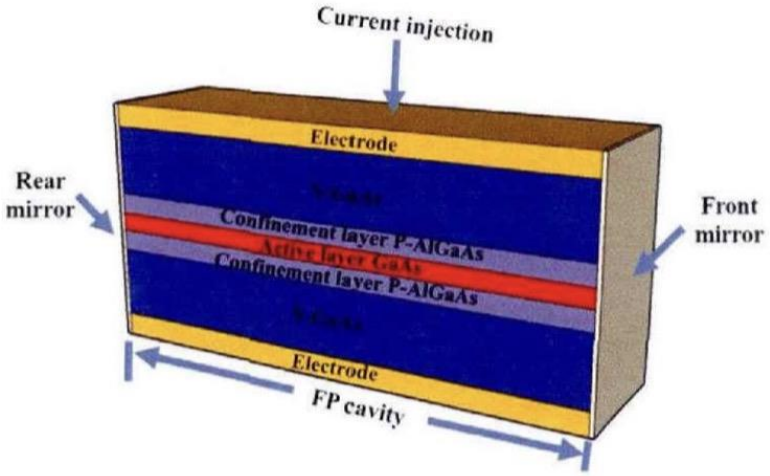

Figure 1.1 Schematic structure of FP-LD

As shown in Fig. 1.1, the mirrored ends of the FP-LD (typically a highly reflective coating) form the laser's resonant cavity. When light waves reflect back and forth within this cavity, they can be amplified by the gain medium between the mirrors. If the gain exceeds the losses, laser output can be achieved.

To achieve lasing, the FP-LD requires not only that the injected current exceeds the threshold but also that the emitted light satisfies certain phase conditions, namely:

$$kL = m\pi, m = 1,2,3 \ldots \tag{1.1}$$

where k is the wave vector, and $k = 2\pi n_{eff}/\lambda$, n_{eff} is the effective refractive index of the active region, and L is the length of the laser cavity. By substituting these into Eq 1.1, we can further deduce the condition that the lasing wavelength must satisfy:

$$2n_{eff}L = m\lambda, m = 1,2,3 \ldots \tag{1.2}$$

From Eq. (1.2), we understand that each m corresponds to a lasing mode, indicating that the FP-LD is capable of multi-wavelength lasing. Moreover, when the effective refractive index (n_{eff}) is constant, the spacing between lasing wavelengths (i.e., mode spacing) of the FP-LD is determined by the cavity length (L). When $m \gg 1$, the mode spacing can be expressed as:

$$\Delta\lambda = \lambda_m - \lambda_{m+1} \approx \frac{2n_{eff}L}{m(m+1)} \approx \frac{\lambda_m^2}{2n_{eff}L}. \tag{1.3}$$

The corresponding frequency difference, Δf, can be expressed as:

$$\Delta \mathrm{f} = \frac{\mathrm{c}}{\lambda_{m+1}} - \frac{\mathrm{c}}{\lambda_m} \approx \frac{c}{2n_{eff}L}. \tag{1.4}$$

However, meeting the phase condition is merely the primary requirement for FP-LD to achieve lasing. The lasing wavelength of FP-LD is also influenced by the gain characteristics of the active material. The gain characteristic of the active material is not uniform; it is typically represented by a curve, often resembling a Gaussian shape. Therefore, only the modes that are within the high-gain central region can achieve lasing. Due to the multi-mode characteristic of FP-LD, mode competition usually occurs during the lasing process, where modes with relatively higher gains tend to have an advantage. As the injection current of FP-LD gradually increases, a wavelength with a relatively higher gain reaches the threshold gain first, while suppressing other modes, thus achieving single-mode lasing. Similarly, due to the disadvantage of FP-LD's tendency for multi-mode operation, there can be significant RIN during high-speed direct modulation, which is why it is typically used in low to mid-speed optical fiber communication systems.

1.2.2 Distributed-feedback Laser Diode

As mentioned previously, due to the broad spectral line, the spectral response of FP lasers is typically poor. In response to this, Kogelnik and Shank proposed the distributed-feedback laser (DFB) in 1972 [6]. The working principle of this laser is based on a periodic cut-off waveguide (Bragg grating), meaning it does not have aggregated reflective mirrors for its resonant cavity but instead forms feedback through a Bragg grating with a periodic structure. The Bragg grating is fabricated on or within the gain region, usually distributed uniformly within the resonant cavity. Electromagnetic waves within the laser are amplified

by the gain in the active region and then filtered through the Bragg grating for frequency selection, ultimately achieving lasing. If the grating in a DFB laser is uniform, the corresponding Bragg wavelength, λ_B, is:

$$\lambda_B = 2n_{eff}\Lambda_0, \tag{1.5}$$

where n_{eff} is the effective refractive index of the active region, and Λ_0 is the period of the grating.

The DFB-LD can be specifically categorized based on the location of its grating fabrication into index-coupled DFB-LD, gain-coupled DFB-LD, and complex-coupled DFB-LD. Among these, the index-coupled DFB-LD, with its grating fabricated above the active region rather than etched into it, features a simpler manufacturing process and is therefore widely used in the field of optical communications. Fig. 1.2 illustrates the schematic structure of an index-coupled uniform grating DFB-LD. In this diagram, the grating modulates and provides feedback to the light waves within the active region below.

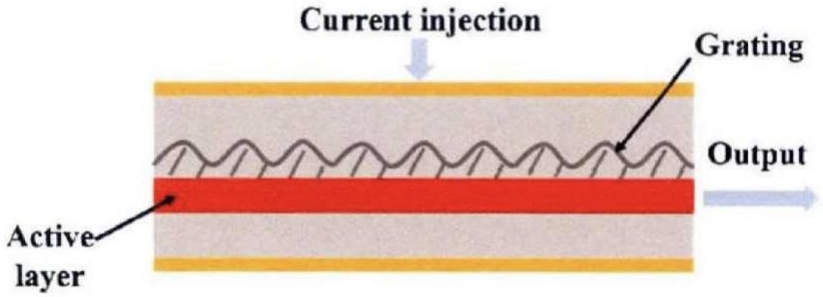

Figure 1.2 Schematic structure of DFB-LD

However, due to the optical characteristics of the uniform grating DFB-LD, it tends to generate degenerate modes at two symmetric positions around the Bragg wavelength, leading to the possibility of multi-mode operation and reducing the yield of high-quality lasers. To address this, a π phase shift is commonly introduced into the center of the grating in industrial applications. This approach effectively eliminates the existing degenerate modes, resulting in stable single-mode lasing.

1.2.3 Distributed Bragg Reflector Laser diode

A simple distributed Bragg reflector laser diode (DBR-LD) structure, as shown in Fig. 1.3, consists of three sections: the left grating region, the gain region, and the right grating region. Unlike the DFB-LD, where the grating is located within or on top of the gain region, the grating regions of a DBR-LD are positioned at one or both ends of the laser resonator. The active region generates photons due to electrical excitation. The Bragg gratings at the

ends select specific frequencies of the amplified light waves. A particular wavelength is then reflected back and forth, oscillating until laser output is achieved.

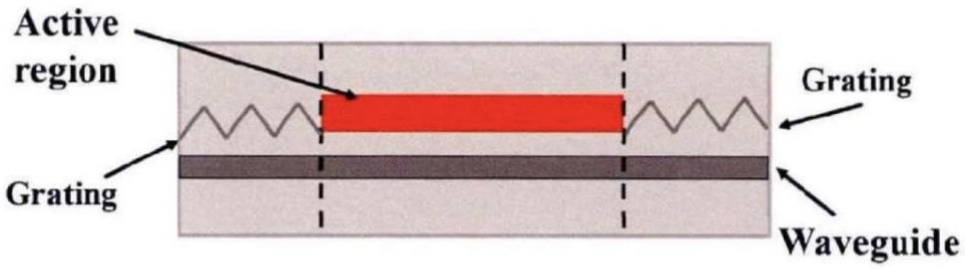

Figure 1.3 Schematic structure of DBR-LD

1.2.4 Vertical Cavity Surface Emitting Laser

In the 1980s, the Japanese scholar K. Iga first fabricated the Vertical Cavity Surface Emitting Laser (VCSEL) [7-9]. After half a century of development, VCSELs have been widely used in various fields such as optical storage and communications. As illustrated in Fig. 1.4, a top-emitting VCSEL consists of resonant cavities formed by upper n-DBR and lower p-DBR mirrors, with one or several quantum wells grown in the middle acting as the gain region. Due to the short cavity length of VCSELs, light waves need to oscillate multiple times between the resonant cavities to achieve lasing. Therefore, thin films with very high reflectivity (>99%) are required to serve as mirrors.

Compared to edge-emitting lasers, VCSELs offer numerous advantages: 1. They have a short resonant cavity, leading to a low threshold current (on the order of 0.1 mA). 2. They

facilitate easy coupling and allow for straightforward device packaging. 3. Their compact size makes them suitable for large-scale photonic integration through arrays.

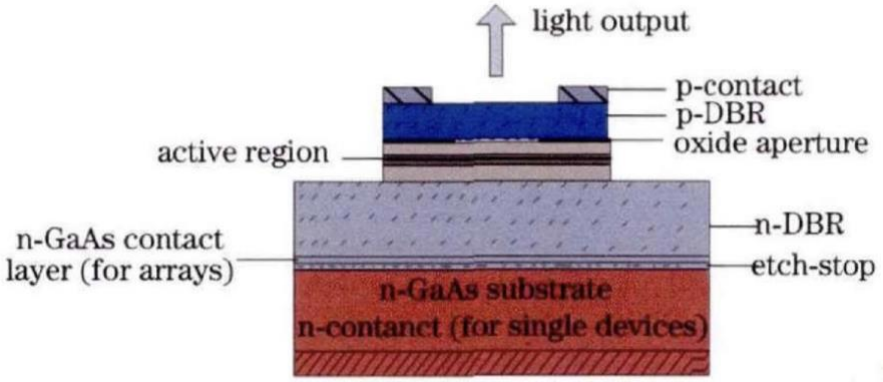

Figure 1.4 Schematic structure of VCSEL

1.3 Research Background

The DFB lasers are widely used in fiber-optic communication systems and networks due to their stable single-mode operation characteristics [10]. However, the randomness in their grating duty-cycles introduced by imperfect fabrication processes, including the grating pattern formation by either electron beam lithography or optical holography, and the grating dry and/or wet etching, can potentially lead to detrimental effects on the device's performance. This is because the disruption on the periodicity of the grating jeopardizes the phase condition required to constructively establish the lasing mode coherence. Despite the possible significant impact of the grating duty-cycle randomness (DCR) on DFB laser performance, there seems to be a lack of systematic study on this topic so far.

Numerical simulation is an efficient and reliable way to tackle this problem for reproducing the grating DCR through experimental approach is costly, and the simulation tools for the DFB lasers are mature and accurate [11]. Many models and associated numerical solution techniques have been developed for DFB laser's static and dynamic performance simulation. To capture the grating effect in the DFB lasers, those one-dimensional (1D) models along the wave propagation direction (i.e., along the laser cavity) are sufficient. In those 1D approaches, there still exist the traveling-wave method (TWM) [12-17] and the standing-wave method (SWM) [18-20]. In principle, either method can be exploited to solve our problem. However, the complex root searching algorithm employed by the SWM often miss the true root or find the false root in dealing with complicated grating structures. The TWM is therefore preferred in our case for it only involves a marching algorithm. Although the coupled-mode equation based TWM [6,21,22] is more popular in dealing with the DFB lasers with "ideal" gratings without randomness, the transfer matrix model (TMM) that deals with the grating in a pitch-by-pitch fashion [23-25] is more suitable for dealing with gratings with DCR. However, current applications of the transfer matrix method primarily simulate perfect grating structures (without DCR). Thus, these methods employ simplification approach for identical matrix multiplication by exploiting matrix diagonalization.

1.4 Contribution and Organization of the Thesis

Similar to those reported methods in the literature [23-25] that divided the grating down to pitches, in this thesis, we firstly developed a modified TMM that breaks the grating all the way down to sub-pitch to capture the DCR from pitch to pitch. Although simulation time would increase, this allows for the inclusion of DCR, yielding more accurate results. This new method has been validated for reliability by comparison with the established SWM. This thesis utilizes this method to simulate and comparatively analyze the impact of DCR on the performance of different types of DFB lasers, including uniform grating, quarter-wavelength phase-shifted DFB lasers, and corrugation-pitch modulation (CPM) grating DFB lasers.

This thesis is organized as follows: Chapter 2 will present the optical field equations and carrier rate equations within the one-dimensional laser model. Starting from Maxwell's equations, the wave equation is derived, followed by the formulation of the equations governing the optical field within the laser. For the distribution of carriers in the active region of semiconductor lasers, this document employs rate equations for a phenomenological description. The treatment of material gain models and spontaneous emission noise sources also utilizes straightforward empirical formulas. Chapter 3 will provide a detailed introduction to the transfer matrix method and demonstrate its application in simulating DFB lasers with DCR. The chapter will derive the frequency-domain transfer matrix equations used to calculate the steady-state characteristics of lasers. Subsequently, modifications will be made to these equations to enable the calculation of the dynamic characteristics of lasers in the time domain. The model is validated by

comparison with that obtained from the well-established standing-wave model. Chapter 4 will present the performance simulation results of DFB lasers with DCR using the above method and will discuss the impact of DCR on the performance of DFB lasers. Chapter 5 summarizes the thesis and gives the research conclusion.

Chapter 2

1D Numerical Models for DFB Lasers

2.1 Optical Field Equations

The optical field in a medium is constrained by Maxwell's equations [11,24], as shown in Eq. (2.1):

$$\nabla \times \vec{E}(\vec{r},t) = -\frac{\partial}{\partial t}\vec{B}(\vec{r},t), \tag{2.1a}$$

$$\nabla \times \vec{H}(\vec{r},t) = \frac{\partial}{\partial t}\vec{D}(\vec{r},t) + \vec{J}(\vec{r},t), \tag{2.1b}$$

$$\nabla \cdot \vec{D}(\vec{r},t) = \rho(\vec{r},t), \tag{2.1c}$$

$$\nabla \cdot \vec{B}(\vec{r},t) = 0, \tag{2.1d}$$

where $\vec{E}$ and $\vec{H}$ represent the electric and magnetic field vectors in [V/m] and [A/m], respectively. $\vec{D}$ and $\vec{B}$ denote the electric flux density and magnetic flux density in [C/m^2] and [Wb/m^2], respectively. $\vec{J}$ and ρ denote the current density and charge density in [[A/m^2] and [C/m^3], respectively. $\vec{r}$ and t represent the spatial coordinate vector and the time variable.

In dielectric materials, the constitutive relations are as follows:

$$\vec{D} = \vec{\varepsilon}\vec{E} = \varepsilon_0\vec{E} + \vec{P}, \tag{2.2a}$$

$$\vec{B} = \vec{\mu}\vec{H} = \mu_0\vec{H} + \vec{M}, \tag{2.3b}$$

where $\vec{P}$ and $\vec{M}$ represent the electric polarization and magnetic polarization intensities of the material, respectively. $\vec{\varepsilon}$ and $\vec{\mu}$ are the material's dielectric constant and magnetic permeability.

Assuming the material is isotropic, the dielectric constant ε and magnetic permeability μ are scalar values. In semiconductor lasers, the following conditions apply: 1) For the electromagnetic field at the optical frequency, assume $\rho = 0$; 2) In the passive region, set $\vec{J} = 0$; 3) In the active region, due to spontaneous emission, set $\vec{J} = \overrightarrow{J_{sp}}$.

By substituting Eq. (2.2) into Eq. (2.1) and following a series of mathematical derivations, the wave equation can be derived as follows:

$$\vec{B} = \vec{\mu}\vec{H},$$

$$\nabla \times \left(\frac{1}{\mu}\vec{B}\right) = \nabla \times \vec{H},$$

$$\frac{\partial}{\partial t}\nabla \times \left(\frac{1}{\mu}\vec{B}\right) = \frac{\partial}{\partial t}\nabla \times \vec{H},$$

$$\nabla \times \left(\frac{1}{\mu}\frac{\partial}{\partial t}\vec{B}\right) = \frac{\partial}{\partial t}\nabla \times \vec{H},$$

$$-\nabla \times \left(\frac{1}{\mu}\nabla \times \vec{E}\right) = \frac{\partial}{\partial t}\nabla \times \vec{H},$$

$$\nabla \times \left(\frac{1}{\mu}\nabla \times \vec{E}\right) + \frac{\partial}{\partial t}\nabla \times \vec{H} = 0.$$

This results in the following equation:

$$\nabla \times \left(\frac{1}{\mu}\nabla \times \vec{E}\right) + \varepsilon \frac{\partial^2}{\partial t^2}\vec{E} + \frac{\partial}{\partial t}\vec{J} = 0. \tag{2.3}$$

Due to:

$$\nabla \times \left(\frac{1}{\mu}\nabla \times \vec{E}\right) = \frac{1}{\mu}\nabla \times \left(\nabla \times \vec{E}\right) + \left(\nabla \frac{1}{\mu}\right) \times \left(\nabla \times \vec{E}\right),$$

$$\nabla \times \left(\nabla \times \vec{E}\right) = \nabla \times \left(\nabla \cdot \vec{E}\right) - \nabla^2 \vec{E}.$$

Consequently, from Eq. (2.3) we derive Eq. (2.4):

$$\nabla^2 \vec{E} - \mu\varepsilon \frac{\partial^2}{\partial t^2}\vec{E} + (\nabla ln\mu) \times \left(\nabla \times \vec{E}\right) - \nabla \times \left(\nabla \cdot \vec{E}\right) - \mu \frac{\partial}{\partial t}\vec{J} = 0. \tag{2.4}$$

Furthermore, from:

$$\nabla\left(\varepsilon \cdot \vec{E}\right) = \varepsilon \nabla \cdot \vec{E} + \vec{E} \cdot \nabla\varepsilon,$$

$$\nabla ln\varepsilon = \frac{1}{\varepsilon}\nabla\varepsilon = -\varepsilon \nabla \frac{1}{\varepsilon}.$$

We obtain:

$$\nabla^2 \vec{E} - \mu\varepsilon \frac{\partial^2}{\partial t^2}\vec{E} + (\nabla ln\mu) \times \left(\nabla \times \vec{E}\right) + \nabla\left(\vec{E} \cdot \nabla ln\varepsilon\right) - \mu \frac{\partial}{\partial t}\vec{J} = 0. \tag{2.5}$$

For the magnetic field $\vec{H}$, there is an expression similar to Eq. (2.5), as shown in Eq. (2.6):

$$\nabla^2 \vec{H} - \mu\varepsilon \frac{\partial^2}{\partial t^2}\vec{H} + (\nabla ln\varepsilon) \times \left(\nabla \times \vec{H}\right) + \nabla\left(\vec{H} \cdot \nabla ln\mu\right) + \nabla \times \vec{J} + \vec{J} \times \nabla ln\mu = 0. \tag{2.6}$$

In a homogeneous isotropic medium, $\nabla ln\varepsilon = 0$ and $\nabla ln\mu = 0$, Eq. (2.5) and (2.6) can be simplified to:

$$\nabla^2 \vec{E} - \mu\varepsilon \frac{\partial^2}{\partial t^2}\vec{E} - \mu \frac{\partial}{\partial t}\vec{J} = 0, \tag{2.7}$$

$$\nabla^2\vec{H} - \mu\varepsilon\frac{\partial^2}{\partial t^2}\vec{H} + \nabla\times\vec{J} = 0. \tag{2.8}$$

Considering the equivalence of electric and magnetic fields in electromagnetic fields, it is sufficient to calculate the electric field alone to obtain all the information about the electromagnetic field:

$$\nabla^2\vec{E} = \mu\varepsilon\frac{\partial^2}{\partial t^2}\vec{E} + \mu\frac{\partial}{\partial t}\vec{J}. \tag{2.9}$$

Compared to Maxwell's Eq. (2.1), the wave Eq. (2.9) more directly reflects the relationships that the electric field must satisfy, and significantly reduces the number of unknowns in the equation. However, Eq. (2.9) is a second-order hyperbolic partial differential equation, which differs from elliptic and parabolic partial differential equations primarily because its eigen solutions appear in the form of simple harmonic oscillations. The solutions to Eq. (2.9) can be viewed as simple harmonic waves modulated by a slowly varying envelope, as shown in Eq. (2.10).

$$\vec{E}(\vec{r},t) = \frac{1}{2}\Sigma_k\overrightarrow{u_k}(\vec{r},t)e^{-j\omega_k t} + c.c. \tag{2.10}$$

In Eq. (2.10), the optical wave is considered as a linear superposition of simple harmonic waves of different frequencies. Here, $\overrightarrow{u_k}$ is the slowly varying envelope corresponding to the k -th harmonic, in [V/m]; ω_k represents the angular frequency of the k -th harmonic, in [rad/s]; $c.c.$ denotes the complex conjugate. In subsequent sections, it is assumed that $c.c.$ is omitted in expressions related to the optical field. The occurrence of $e^{-j\omega_k t}$ in Eq. (2.10) serves to reduce the time derivative from a second order to a first order derivative.

Representing the solution of Eq. (2.9) in the form of Eq. (2.10) can be seen as a reduction of the wave equation in the time domain.

Mathematically, the time and space variables hold equivalent status in Eq. (2.9). Following the previously discussed method of reducing the time derivative, a similar reduction can be applied to the spatial variables, converting the second-order spatial derivatives to first-order derivatives. Consequently, Eq. (2.10) can be further expressed as Eq. (2.11).

$$\vec{E}(\vec{r},t) = \Sigma_k \overrightarrow{v_k}(\vec{r},t) e^{j\beta_k z} e^{-j\omega_k t}, \tag{2.11}$$

where $\overrightarrow{v_k}$ represents the slowly varying envelope of the k -th plane wave, in [V/m]; β_k denotes the propagation constant of the k -th plane wave, in [rad/m].

In semiconductor DFB lasers, it is commonly assumed that the variation in the optical field distribution across the cross-section is minimal and can be approximated as uniform. This implies that the components of $\overrightarrow{v_k}(\vec{r},t)$ in the x and y directions, as mentioned in Eq. (2.11), are considered time-invariant. Consequently, Eq. (2.11) can be further rewritten as Eq. (2.12).

$$\vec{E}(\vec{r},t) = \vec{s}\phi(x,y)e(z,t)e^{j(\beta_0 z - \omega_0 t)}. \tag{2.12}$$

where $\vec{s}$ represents the unit vector of the polarization direction of the optical field $\vec{E}$. This study only analyzes the TE mode, hence here $\vec{s}$ denotes $\overrightarrow{x}$. The term $\phi(x,y)$ describes the distribution of the optical field across the cross-section, in [1/m], and is considered constant along the longitudinal, or z direction, termed as the mode distribution of the optical waveguide. The function $e(z,t)$ represents the envelope of the optical field along the z

direction, which varies slowly with time and position, in [V]. The term $e^{j(\beta_0 z-\omega_0 t)}$ also represents the phase coefficient, which is dimensionless. Due to the linear superposition of harmonics, Eq. (2.12) only presents the expression corresponding to ω_0 and omits the complex conjugate terms.

In Eq. (2.12), the optical field $\vec{E}$ is considered to have a stable distribution across the cross-section that does not vary with time. Along the longitudinal z direction, it is represented as a simple harmonic plane wave. Therefore, the expression in Eq. (2.12) should differentiate between the +z and −z directions, leading to a reformulation of Eq. (2.12) into Eq. (2.13).

$$\vec{E}(x,y,z,t) = \vec{s}\phi(x,y)\left[e^{f}(z,t)e^{j\beta_0 z} + e^{r}(z,t)e^{-j\beta_0 z}\right]e^{-j\omega_0 t}, \tag{2.13}$$

where e^{f} represents the forward component of the slowly varying envelope of the field, and e^{r} represents the backward component.

By substituting Eq. (2.13) into Eq. (2.9), the constraint equation for the mode field distribution across the cross-section can be derived, as shown in Eq. (2.14).

$$\left(\frac{\partial^2}{\partial x^2}+\frac{\partial^2}{\partial y^2}\right)\phi(x,y) + k_0^2 n^2(x,y)\phi(x,y) = \beta_0^2\phi(x,y). \tag{2.14}$$

Regarding the longitudinal optical field distribution described by $\left[e^{f}(z,t)e^{j\beta_0 z} + e^{r}(z,t)e^{-j\beta_0 z}\right]$, the propagation of e^{f} and e^{r} within the DFB laser cavity can be

effectively illustrated as in Fig. 2.1, where n_a and n_b respectively represent the high and low effective refractive indices of the grating.

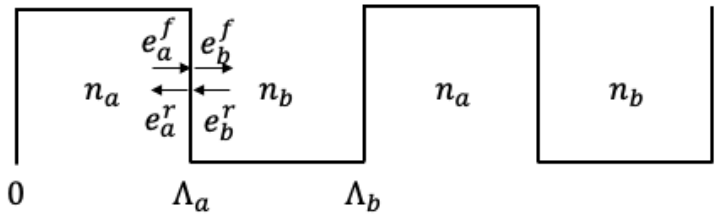

Figure 2.1 Schematic of optical field in DFB grating

In Figure 2.1, in conjunction with Eq. (2.13), for the TE mode, the electric field component Ey within the grating section Λ_s can be expressed by Eq. (2.15).

$$e_{ys} = \left[e_s^f e^{-j\beta_0 z} + e_s^r e^{j\beta_0 z}\right]\phi_s(x,y) + e_s^{rad}\ (s = a, b), \tag{2.15}$$

where e_s^{rad} represents the radiation mode in [V].

At the interface where $z = \Lambda_a$, based on the boundary conditions of the electric field component Ey and the magnetic field component Hx, the following equation can be derived:

$$\left(e_a^f + e_a^r\right)\phi_a(x,y) + e_a^{rad} = \left(e_b^f + e_b^r\right)\phi_b(x,y) + e_b^{rad}, \tag{2.15a}$$

$$-j\beta_a\left(e_a^f - e_a^r\right)\phi_a(x,y) + \frac{\partial}{\partial z}e_a^{rad} = -j\beta_b\left(e_b^f - e_b^r\right)\phi_b(x,y) + \frac{\partial}{\partial z}e_b^{rad}. \tag{2.16b}$$

By multiplying both sides of Eq. (2.16) by $\phi_a(x,y)$ and integrating over the cross-section, Eq. (2.17) can be derived.

$$\begin{bmatrix} e_a^f \\ e_a^r \end{bmatrix} = \begin{bmatrix} \frac{\beta_a + \beta_b}{2\beta_a}\chi_{ab} & \frac{\beta_a - \beta_b}{2\beta_a}\chi_{ab} \\ \frac{\beta_a - \beta_b}{2\beta_a}\chi_{ab} & \frac{\beta_a + \beta_b}{2\beta_a}\chi_{ab} \end{bmatrix} \begin{bmatrix} e_b^f \\ e_b^r \end{bmatrix}, \tag{2.17}$$

$$\chi_{ab} = \frac{\int \phi_a \phi_b dxdy}{\int \phi_a^2 dxdy}. \tag{2.18}$$

In Eq. (2.17), the contribution of e^{rad} to the first-order grating is very small and is therefore considered negligible. χ_{ab} represents the overlap of the mode field distributions within n_a and n_b . If the effective refractive indices n_a and n_b are defined as $n_a = \beta_a/k$ and $n_b = \beta_b/k$, where $k = 2\pi/\lambda$ is the wave vector in vacuum, then Eq. (2.17) can be rewritten as follows:

$$\begin{bmatrix} e_a^f \\ e_a^r \end{bmatrix} = \begin{bmatrix} 1/t_{ab} & r_{ab}/t_{ab} \\ r_{ab}/t_{ab} & 1/t_{ab} \end{bmatrix} \begin{bmatrix} e_b^f \\ e_b^r \end{bmatrix}, \tag{2.19a}$$

$$t_{ab} = \frac{2n_a}{n_a + n_b} \cdot \frac{1}{\chi_{ab}}, \tag{2.19b}$$

$$r_{ab} = \frac{n_a - n_b}{n_a + n_b}. \tag{2.19c}$$

Similar, we can obtain:

$$\begin{bmatrix} e_b^f \\ e_b^r \end{bmatrix} = \begin{bmatrix} 1/t_{ba} & r_{ba}/t_{ba} \\ r_{ba}/t_{ba} & 1/t_{ba} \end{bmatrix} \begin{bmatrix} e_a^f \\ e_a^r \end{bmatrix}. \tag{2.20}$$

In Figure 2.1, for the uniform sections from $z = 0$ to $z = \Lambda_a$ or from $z = \Lambda_a$ to $z = \Lambda_b$, the expression for the transfer matrix can be written as follows:

$$T_s = \begin{bmatrix} e^{-j\beta_s \Lambda_s} & 0 \\ 0 & e^{j\beta_s \Lambda_s} \end{bmatrix}, \quad (s = a, b) \tag{2.21}$$

The transfer matrix for the entire grating structure can be obtained by the product of the transfer matrices of each section, as shown in the following equation:

$$\begin{bmatrix} e^{f}_{z=L} \\ e^{r}_{z=L} \end{bmatrix} \tag{2.22}$$

$$= \begin{bmatrix} 1/t_{ab} & r_{ab}/t_{ab} \\ r_{ab}/t_{ab} & 1/t_{ab} \end{bmatrix} \begin{bmatrix} e^{-j\beta_b \Lambda_b} & 0 \\ 0 & e^{j\beta_b \Lambda_b} \end{bmatrix} \begin{bmatrix} 1/t_{ba} & r_{ba}/t_{ba} \\ r_{ba}/t_{ba} & 1/t_{ba} \end{bmatrix} \begin{bmatrix} e^{-j\beta_a \Lambda_a} & 0 \\ 0 & e^{j\beta_a \Lambda_a} \end{bmatrix} \begin{bmatrix} e \\ e \end{bmatrix}$$

$$= \begin{bmatrix} T_{11} & T_{12} \\ T_{21} & T_{22} \end{bmatrix} \begin{bmatrix} e^{f}_{z=0} \\ e^{r}_{z=0} \end{bmatrix}.$$

Let $e^{f}_{z=0} = 1, e^{r}_{z=L} = 0$, we obtain:

$$t = \frac{e^{f}_{z=L}}{e^{f}_{z=0}} = \frac{T_{11} \cdot T_{22} - T_{22} \cdot T_{21}}{T_{22}}, \tag{2.23}$$

$$r = \frac{e^{r}_{z=0}}{e^{f}_{z=0}} = -\frac{T_{21}}{T_{22}}. \tag{2.24}$$

2.2 Carrier Rate Equation

The carrier rate equations include terms for both the generation rate and recombination rate of carriers. Carrier generation primarily arises from the injection of external current; however, carrier recombination is more complex, involving direct recombination that emits photons, Shockley-Read-Hall recombination, and various types of Auger recombination, among others. Clearly, to ensure energy conservation, the rate of change in carrier concentration within the optical cavity must equal the generation rate minus the recombination rate. A phenomenological expression for this process is given in Eq. (2.25).

$$\frac{\partial}{\partial t}N(z,t) = \frac{\eta I(z,t)}{eV} - \Gamma g v_g S - \frac{N}{\tau}. \tag{2.25}$$

where N represents the carrier concentration in the active region of the laser, in [1/m^3]; I represents the injected current, in [A]; η is the injection efficiency, dimensionless; V represents the volume of the active region, in [m^3]; e represents the elementary charge of an electron, in [C]; S represents the photon density in the active region, in [1/m^{-3}]; τ represents the carrier lifetime, with units of [s]; g represents the material gain in the active region, in [1/m].

In Eq. (2.25), the first term on the right-hand side represents the rate of carrier generation due to current injection, where $\eta I/eV$ calculates the number of electrons per unit volume in the active region, and I denotes the current injected at the surface of the laser electrode, with η typically around 40%. The second term accounts for carriers recombined through stimulated emission, which is directly proportional to the photon density and the spectral gain. The third term accounts for carriers consumed by processes including spontaneous emission and various types of Auger recombination. The $\frac{N}{\tau}$ term encompasses several recombination mechanisms, as detailed in Eq. (2.26):

$$\frac{N}{\tau} = AN + B(NP) + C'(N^2P) + C''(NP^2). \tag{2.26}$$

In Eq. (2.26), the first term on the right side represents non-radiative recombination, the rate of which is directly proportional to the electron concentration N, with a proportionality constant A, in [1/s]. The second term denotes bimolecular radiative recombination, proportional to both the electron concentration N and the hole concentration P, with a

constant B, in [m^3/s]. The last two terms represent various Auger recombination processes, with a constant C, in [m^6/ s]. It is typically assumed that the charge in the active region is electrically neutral, meaning the electron and hole concentrations are equal. Consequently, Eq. (2.26) can be rewritten as Eq. (2.27):

$$\frac{N}{\tau} = AN + BN^2 + CN^3. \tag{2.27}$$

By substituting Eq. (2.27) into Eq. (2.25), the following can be derived:

$$\frac{\partial}{\partial t}N(z,t) = \frac{\eta I(z,t)}{eV} - [AN(z,t) + BN^2(z,t) + CN^3(z,t)] - \Gamma g(z,t) v_g S(z,t). \tag{2.28}$$

Based on the distribution of the optical field, the distribution of the photon density can be calculated, as shown in Eq. (2.29):

$$S(z,t) = \frac{\left[\frac{n_{eff}}{2}\sqrt{\frac{\varepsilon_0}{\mu_0}}\left(\left|e^f(z,t)\right|^2 + \left|e^r(z,t)\right|^2\right)\right]/\hbar\omega_0}{v_g \Sigma ar}. \tag{2.29}$$

where n_{eff} represents the effective refractive index within the laser waveguide; v_g denotes the group velocity, in [m/s]; Σar represents the cross-sectional area of the active region, in [m^2]; $\hbar\omega_0$ denotes the energy of a single photon at the reference frequency, in [J].

2.3 Material Gain

Osinski M. and Adams M. J. [26] proposed that the material gain is linearly related to the carrier concentration, and the expression is as follows:

$$g = g_N^{Bulk}(N - N_{tr}). \tag{2.30}$$

where g_N^{Bulk} represents the material gain coefficient of the bulk material structure, in [m^2]; N_{tr} denotes the transparency carrier concentration, in [m^{-3}]. The approximation of Eq. (2.30) is reasonable when the injected current is near the threshold current.

For DFB lasers with multi-quantum well structures, the material gain no longer exhibits a linear relationship with carrier concentration but instead follows a logarithmic relationship, as illustrated in Eq. (2.31):

$$g = g_N^{MQW}\ln(N/N_{tr}) \tag{2.31}$$

where g_N^{MQW} represents the material gain coefficient for multi-quantum well structures, in [1/m].

As the injection current approaches the threshold value, the carrier concentration increases with the increase in injection current, and the relationship between material gain and carrier concentration can still be approximated linearly. However, as the injection current continues to increase, the material gain and carrier concentration will no longer increase linearly but will exhibit gain saturation. Using multi-quantum well structures as an example, this introduces the phenomenon of material gain saturation, and the expression for material gain is modified as follows:

$$g = \frac{g_N^{MQW}\ln(N/N_{tr})}{1 + \epsilon S}. \tag{2.32}$$

2.4 Spontaneous Emission Noise Source

This thesis addresses the treatment of spontaneous emission noise sources using a phenomenological empirical model.

The optical field $e(z)$ progresses to point $e(z+dz)$ after a time interval dt. This process is represented as:

$$e(z+dz) = e^{\left[jk_0\Delta n+\frac{1}{2}(\Gamma g-\alpha_L)\right]dz}e(z) + s(z)dz. \tag{2.33}$$

Since the phase of spontaneous emission noise is random, the amplitude power is of greater interest. By multiplying the previous equation by its complex conjugate and a factor $\frac{n_{eff}}{2}\sqrt{\frac{\varepsilon_0}{\mu_0}}$ with units of $1/\Omega$, the result is expressed as Eq. (2.34):

$$P(z+dz) = e^{(\Gamma g-\alpha_L)dz}P(z) + \frac{n_{eff}}{2}\sqrt{\frac{\varepsilon_0}{\mu_0}}|s(z)|^2dz^2. \tag{2.34}$$

In Eq. (2.34), the second term on the right side represents the contribution of spontaneous emission noise sources to the power of the optical field as it changes from $e(z)$ to $e(z+dz)$. This can be phenomenologically expressed as:

$$\frac{n_{eff}}{2}\sqrt{\frac{\varepsilon_0}{\mu_0}}|s(z)|^2dz^2 = \gamma v_g\Gamma g\hbar\omega_0. \tag{2.35}$$

From Eq. (2.35), we can derive:

$$|s(z)|^2 = \frac{2}{n_{eff}}\sqrt{\frac{\mu_0}{\varepsilon_0}}\gamma v_g \Gamma g \hbar \omega_0 \frac{1}{dz^2}. \tag{2.36}$$

After substituting v_g/dz with $1/dt$, the equation can be rewritten as follows:

$$|s(z)|^2 = \frac{2}{n_{eff}}\sqrt{\frac{\mu_0}{\varepsilon_0}}\gamma v_g \Gamma g \hbar \omega_0 \frac{1}{dz}\frac{1}{dt}. \tag{2.37}$$

As a Langevin noise source, both the amplitude and phase can be represented by random numbers from Gaussian and uniform distributions, respectively.

The autocorrelation function of a zero-mean Gaussian random distribution is given by:

$$\langle |s(z,t)||s(z',t)| \rangle = \frac{2}{n_{eff}}\sqrt{\frac{\mu_0}{\varepsilon_0}}\gamma \Gamma g \hbar \omega_0 \delta(z-z')\delta(t-t'). \tag{2.38}$$

Chapter 3

Numerical Solution Based on Time-domain Transfer Matrix Method

3.1 The Modified TMM and Numerical Solution Technique

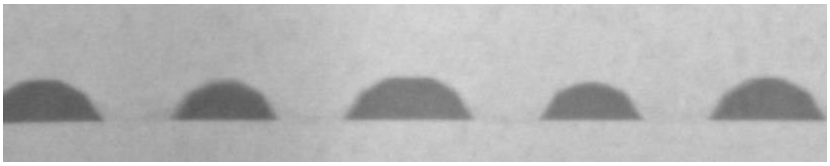

(a)

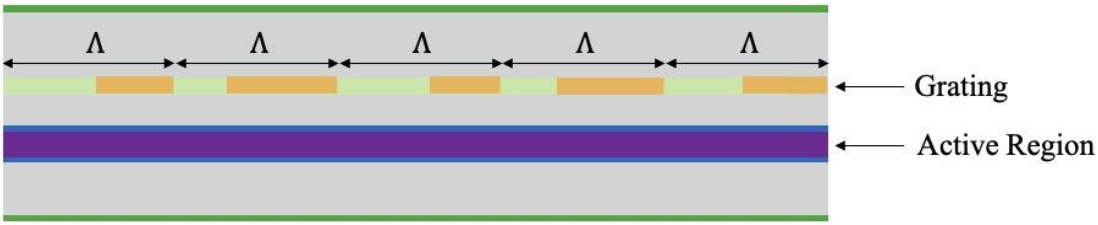

(b)

Figure 3.1. (a) The image of a grating with random duty-cycles due to fabrication imperfection and (b) The schematic diagram of a 1D DFB laser model with grating DCR

Fig. 3.1. (a) shows the image of a fabricated grating in a typical DFB laser, where the grating DCR can clearly be seen. The schematic diagram of a 1D DFB laser model is given as Fig. 3.1. (b), which has a fixed grating period Λ, but the grating duty cycle within each period is random.

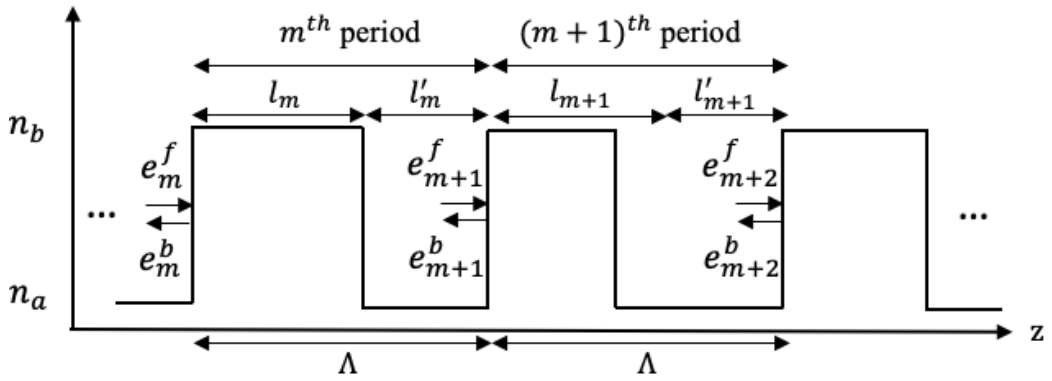

Figure 3.2. The schematic diagram of optical wave propagation in a grating with DCR

Fig. 3.2 shows partial DFB grating with DCR, comprising two periods labeled as m and $m+1$. To treat wave propagation in DFB lasers as described by Eq. (3.1) with its solution taking the form of Eq. (3.2), by following the TMM [23-25], we further divide each grating period into 4 subsections: an interface between two sections with effective indices n_a and n_b, respectively, a smooth waveguide section with effective index n_b and a length of l_{m}, another interface between n_b and n_a, and a smooth waveguide section with n_a and a length of l'_m, as illustrated by Fig. 3.2. Due to the grating DCR, we must let the lengths of the smooth waveguides with effective indices n_b and n_a vary randomly but keep their summation to be fixed as Λ. Since the multiplication of the 4 subsections is different from period to period, no simplification approach for identical matrix multiplication by exploiting matrix diagonalization can be applied, which leaves us a substantially increased burden on numerical computation. Fortunately, such a problem can still be handled by a personal computer.

By letting e_m^f and e_m^b the forward and backward propagating wave amplitude at the lefthand side of the m[th] period, $e_{\mathrm{m+1}}^f$ and $e_{\mathrm{m+1}}^b$ the forward and backward propagating wave amplitude at the righthand side of the m[th] period, (which are also the forward and backward propagating wave amplitudes at the lefthand side of the (m+1)[th] period,) we can express these amplitudes as [25]:

$$\begin{bmatrix} e_{m+1}^f \\ e_{m+1}^b \end{bmatrix} = \begin{bmatrix} e^{-j\beta_{\mathrm{a}} l_m'} & 0 \\ 0 & e^{j\beta_{\mathrm{a}} l_m'} \end{bmatrix} \frac{1}{t_{ab}} \begin{bmatrix} 1 & -r \\ -r & 1 \end{bmatrix} \begin{bmatrix} e^{-j\beta_{\mathrm{b}} l_m} & 0 \\ 0 & e^{j\beta_{\mathrm{b}} l_m} \end{bmatrix} \frac{1}{t_{ba}} \begin{bmatrix} 1 & r \\ r & 1 \end{bmatrix} \begin{bmatrix} e_m^f \\ e_m^b \end{bmatrix}, \quad (3.3a)$$

$$\text{where } r = (n_b - n_a)/(n_b + n_a), t_{ab} = 2n_a/(n_b + n_a), t_{ba} = 2n_b/(n_b + n_a), \quad (3.3b)$$

$$\text{and } \beta_{\mathrm{a,b}} = 2\pi n_{\mathrm{a,b}}/\lambda_0 + (j - \alpha_m)\Gamma g/2 - j\alpha/2, \quad (3.3c)$$

with l_m' , l_m and $\beta_{a,b}$ indicating the lengths and the complex propagation constants of the local guided mode within sections of effective indices n_a and n_b in the m[th] period, respectively.

Defining X as a uniformly distributed random number ranging from 0 to 1, and R ranging from 0 to 100% as a given fixed parameter describing the extent of the randomness, we have:

$$l_m = \Lambda[0.5 + (X - 0.5)R] \text{ and } l_m' = \Lambda - l_m. \quad (3.4)$$

Finally, the optical amplitudes at the laser facets can be connected by sequentially multiplying the amplitude at the very left end with all the matrices in order from left to right:

$$\begin{bmatrix} e_L^f \\ e_L^b \end{bmatrix} = A_L A_M \cdots A_m A_{m-1} \cdots A_2 A_1 A_0 \begin{bmatrix} e_0^f \\ e_0^b \end{bmatrix}, \tag{3.5a}$$

$$\text{where } A_m = \tag{3.5b}$$

$$\begin{bmatrix} e^{-j\beta_a l'_m} & 0 \\ 0 & e^{j\beta_a l'_m} \end{bmatrix} \frac{1}{t_{ab}} \begin{bmatrix} 1 & -r \\ -r & 1 \end{bmatrix} \begin{bmatrix} e^{-j\beta_b l_m} & 0 \\ 0 & e^{j\beta_b l_m} \end{bmatrix} \frac{1}{t_{ba}} \begin{bmatrix} 1 & r \\ r & 1 \end{bmatrix},$$

$$\text{and } A_0 = \frac{1}{\sqrt{1-r_0^2}} \begin{bmatrix} 1 & r_0 \\ r_0 & 1 \end{bmatrix}, A_L = \frac{1}{\sqrt{1-r_L^2}} \begin{bmatrix} 1 & -r_L \\ -r_L & 1 \end{bmatrix}, \tag{3.5c}$$

with r_0 and r_L representing the reflectivity of the left and right facet, respectively, e_0^f and e_0^b the optical amplitudes at the left facet, e_L^f and e_L^b the optical amplitudes at the right facet.

The carrier rate equation that links the injection current density and the carrier density, and the gain model that links the carrier density to the material gain are given as [11]:

$$\frac{\partial N(z,t)}{\partial t} = \eta \frac{J(z,t)}{ed} - [AN(z,t) + BN^2(z,t) + CN^3(z,t)] - v_g g(z,t) S(z,t), \tag{3.6}$$

$$g(z,t) = \frac{g_N [N(z,t) - N_T]}{2[1 + \varepsilon S(z,t)]}, \tag{3.7}$$

with the photon density in Eq. (3.6) and (3.7) defined as [27]:

$$S(z,t) = \frac{n_{eff} \sqrt{\frac{\varepsilon_0}{\mu_0}} \left[\left| e^f(z,t) \right|^2 + |e^b(z,t)|^2 \right]}{2 v_g \Sigma_{ar} \hbar \omega_0}. \tag{3.8}$$

Finally, the output optical power can be found as [11]:

$$Power(L,t) = n_{eff}(1-|r_L|^2)\left|e^f(L,t)\right|^2 / \quad (3.9a)$$

$$2\sqrt{\mu_0/\varepsilon_0},$$

$$Power(0,t) = n_{eff}(1-|r_0|^2)|e^b(0,t)|^2 / \quad (3.9b)$$

$$2\sqrt{\mu_0/\varepsilon_0},$$

with $Power(L,t)$ and $Power(0,t)$ representing the output optical power from the right and left facet, respectively.

In above equations and expressions, we have the following definitions:

g - material gain in [1/m]

N - carrier density inside the active region in [1/m^3]

J - injection current density in [A/m^2]

S - photon density in [1/m^3]

η - injection efficiency, dimensionless

A - nonradiative carrier recombination rate through SRH process in [1/s]

B - carrier recombination coefficient through spontaneous emission and bimolecular processes in [m^3/s]

C - Auger recombination coefficient in [m^6/s]

d - active-region thickness in [m]

e - elementary charge in [C]

$v_g = c/n_g$ - group velocity in [m/s], with n_g indicating the group index

g_N - differential gain [m^2]

N_T - transparency carrier density in [1/m^3]

ε - nonlinear gain saturation factor in [m^3]

Γ - optical confinement factor, dimensionless

α - internal optical loss in [1/m^3]

Σ_{ar} - active-region cross-sectional area in [1/m^2]

$\hbar\omega_0 = hc/\lambda_0$ - single photon energy in [J]

α_m - linewidth enhancement factor, dimensionless

By following the TWM, we need to solve the equation through a time-domain marching algorithm so that the complicated root-searching can be avoided. To address the initial values provided on both facets, we must reformulate Eq. 3.3(a) according to [28-30] by letting the wave follow a contra-propagation scheme in accordance with the time sequence. The use of the time-domain TMM (TD-TMM) is different from the above mentioned steady-state model where the objective was to obtain the overall transfer matrix for the structure (given by the product of the section transfer matrices) from which the oscillation characteristics were determined. However, in TD-TMM, the emphasis is on describing the operation of the individual sections themselves where incrementing the model in time involves updating the traveling-wave amplitudes as they pass a section.

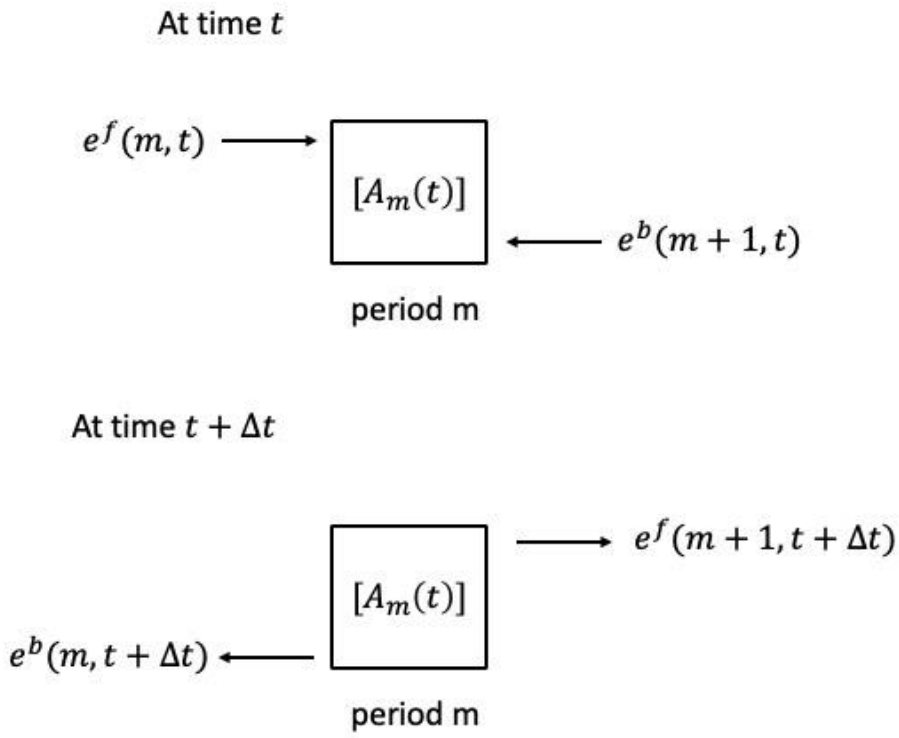

Figure 3.3 Schematic illustrating the use of the transfer matrix $[A_m(t)]$ of a typical period m to update the traveling-wave amplitudes e^f and e^b propagating through the section in a time t to $t+\Delta t$

In the conventional form, the transfer matrix $[A_m]$ of a typical section m expresses the following relationship:

$$\begin{bmatrix} e^f \\ e^b \end{bmatrix}_{m+1} = [A_m] \begin{bmatrix} e^f \\ e^b \end{bmatrix}_m, \tag{3.10}$$

where it relates the amplitudes of the two counterpropagating waves e^f and e^b on either side of the section. Note that in this formulation, steady-state operation has implicitly been assumed.

What is required here is to develop a time-dependent implementation of the TMM. Consider a typical period m at a time t described by the transfer matrix $[A_m(t)]$; see Fig. 3.3. Impinging on the section are the forward and backward-traveling waves $e^f(m,t)$ and $e^b(m+1,t)$. Assuming that $[A_m(t)]$ remains unchanged over the interval t to $t+\Delta t$, Eq. (3.10) can be rewritten as:

$$\begin{bmatrix} e^f(m+1,t+\Delta t) \\ e^b(m+1,t) \end{bmatrix} = [A_m(t)] \begin{bmatrix} e^f(m,t) \\ e^b(m,t+\Delta t) \end{bmatrix} \tag{3.11}$$

$$= \begin{bmatrix} a_{11}(m,t) & a_{12}(m,t) \\ a_{21}(m,t) & a_{22}(m,t) \end{bmatrix} \cdot \begin{bmatrix} e^f(m,t) \\ e^b(m,t+\Delta t) \end{bmatrix}.$$

Writing this out in full gives the following:

$$e^f(+1,t+\Delta t) = a_{11}(m,t)e^f(m,t) + a_{12}(m,t)e^b(m,t+\Delta t) \tag{3.12a}$$

$$e^b(m+1,t) = a_{21}(m,t)e^f(m,t) + a_{22}(m,t)\, e^b(m,t+\Delta t) \tag{3.12b}$$

Rearranging these equations produces expressions for the updated amplitudes in terms of the old wave amplitudes and the transfer matrix elements:

$$e^b(m,t+\Delta t) = [e^b(k+1,t) - a_{21}(m,t)e^f(m,t)]/a_{22}(m,t) \tag{3.13a}$$

$$e^f(m+1,t+\Delta t) = a_{11}(m,t)e^f(m,t) + a_{12}(m,t)\, e^b(m,t+\Delta t) \tag{3.13b}$$

Eq. (3.13) form the basis of the TMM-based dynamic model where it is assumed that the temporal variations in $[A_m]$ and the wave amplitudes occur on a time scale that is negligible in comparison with the optical frequency. At each time increment, the traveling-waves have advanced along the structure by one period, with their amplitudes at the output of each period being updated by the transfer matrix for the period. Essentially, the TMM is employed here to follow the growth and decay of the two traveling waves e^f and e^b as they propagate through the structure.

Our tractable numerical solution technique follows the following procedure: (1) set the injection current; (2) start with an initial traveling wave amplitude distribution at zero and an initial carrier density distribution at transparency; (3) update the carrier density distribution along the cavity by solving (3.6) through the Runge-Kutta method; (4) find the gain distribution from Eq. (3.7); (5) calculate the traveling wave amplitude distribution through the transfer matrix equation in the contra-propagation scheme as shown in Eq. (3.13); (6) find the photon density distribution from Eq. (3.8), which completes one time step; (7) update the traveling wave amplitude distribution with what has been obtained from the previous time step, and repeat (3)~(7) until both traveling wave amplitude distribution and carrier density distributions converge, which gives the steady-state laser performance under the given injection current at step (1). By merging step (1) and (2) to update the injection current at any given time step, we can readily obtain the dynamic laser performance following the above procedure. The final output spectrum is obtained by solving Eq. (3.3) with the gain distribution obtained by the above procedure.

3.2 Model Validation

We validate our model through comparisons made on the device static and dynamic properties with those obtained from the well-established SWM [19] for the same DFB laser structure with the same set of parameters. The devices being investigated are typical DFB lasers with uniform gratings. The modelling parameters are listed in Tab. 3.1. The solid and

dash lines in Fig. 3.4 and 3.5 represent the result calculated by the TMM and SWM, respectively.

Parameters	**Values**
Grating period Λ [nm]	244.5
Active region thickness d $[\mu m]$	0.15
Active-region cross-sectional area Σ_{ar} $[\mu m^2]$	0.3
Facet reflectivity r_1, r_2	0
Laser cavity length L $[\mu m]$	300
Optical confinement factor Γ	0.3
Effective index under zero injection n_{eff}	3.2
Group index n_g	3.6
Optical modal loss α $[cm^{-1}]$	50
Differential gain g_N $[10^{-16}cm^2]$	2.5
Transparent carrier density N_T $[10^{18}cm^{-3}]$	1.0
Nonlinear gain saturation factor ε $[10^{-17}cm^3]$	6.0
Linewidth enhancement factor α_m	4.0
Nonradiative carrier recombination rate through SRH process A $[10^9s^{-1}]$	0.1
Carrier recombination coefficient through spontaneous emission and bimolecular processes B $[10^{-10}cm^3s^{-1}]$	1.0
Auger recombination coefficient C $[10^{-29}cm^6s^{-1}]$	7.5
Grating coupling coefficient $\kappa = \frac{\pi}{\lambda_0}\frac{n_2-n_1}{2}[cm^{-1}]$ [6]	50

Table 3.1 DFB laser parameters used in the validation

1) L-I curve: The static power is obtained by allowing the dynamic response of the laser to reach its steady state for a given bias current. Fig. 3.4 shows the light-current (L-I) curve for this uniform DFB laser. Since the thermal effects are not considered in models, the output power has an almost linear dependency on the injection current, the proposed model shows excellent agreement with the couple mode method along the entire range of current injection.

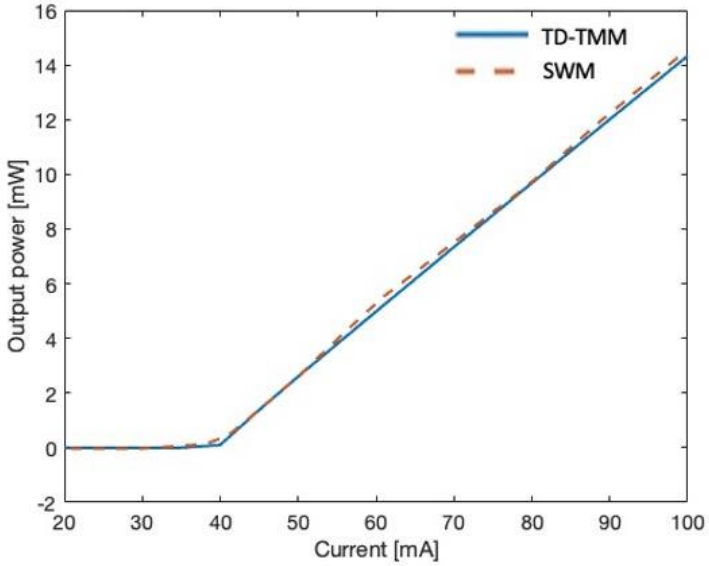

Figure 3.4 Comparison of L-I curve characteristics

2) Longitudinal carrier/photon distributions: Fig. 3.5 (a) and (b) shows the spatial distributions of the carrier and photon densities along the laser cavity, respectively. The agreement between the two models is very good.

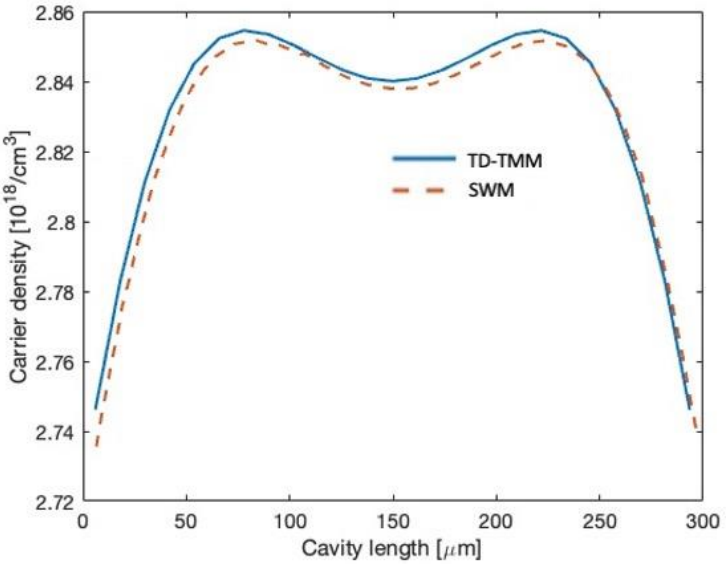

(a)

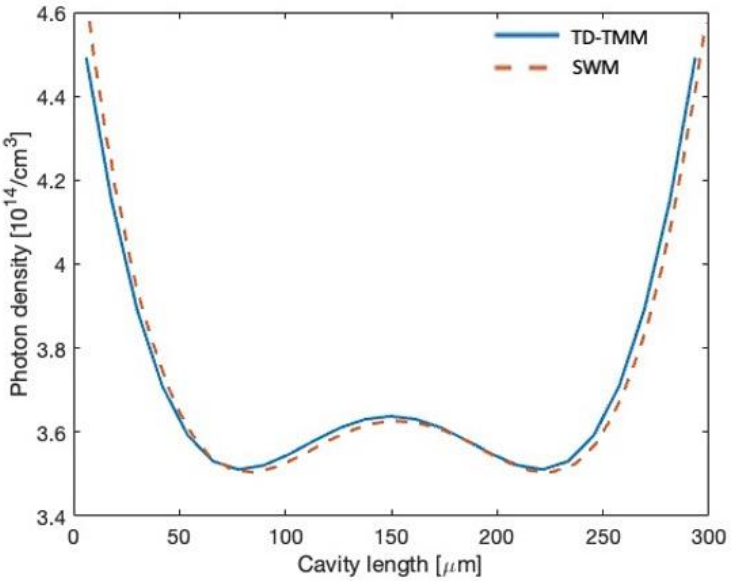

Figure 3.5 Comparison of the longitudinal distributions of (a) carrier density and (b) photon density

Chapter 4

Impact of Grating Duty-Cycle Randomness on DFB Laser Performance

In this section, all laser parameters in simulation are quoted from Tab. 3.1, with the exception that κ is set to different values. κ is introduced in the coupled mode equation model as a measure of the grating coupling strength. In the TMM, the grating coupling strength is altered by the effective index difference between the two sections in each period (i.e., $n_b - n_a$), there is no need to involve κ. However, since κ is a popular design parameter in DFB lasers, we have converted the change on the index contrast ($n_b - n_a$) into the normalized gating coupling coefficient κL with κ given by the formula shown in the bottom row of Tab. 1. As such, instead of the index contrast ($n_b - n_a$), κL is used to indicate the varying of the grating coupling strength. All the DFB laser performance are calculated under a bias current of $I = 60$ mA. The grating is assumed to have a uniformly distributed random variation of its duty-cycle by ±25%.

4.1 Effect of Grating DCR on SMSR

Fig. 4.1 shows the impact of the grating DCR on the SMSR of uniform grating DFB lasers with different κL. The result for DFB lasers with a quarter-wavelength phase-shifted grating at $\kappa L = 2.5$ is also shown for comparison.

The simulation result clearly shows that the SMSR deteriorates significantly. Measured by the median value, the deterioration on SMSR increases from ~5dB at $\kappa L = 3.0$ to ~17dB at $\kappa L = 2.0$ for uniform grating DFB lasers. The quarter-wavelength phase-shifted DFB laser is more immune from the grating DCR as evidenced by only a ~3dB drop of its SMSR at $\kappa L = 2.5$ as compared to a ~12dB drop of the uniform grating DFB laser's SMSR.

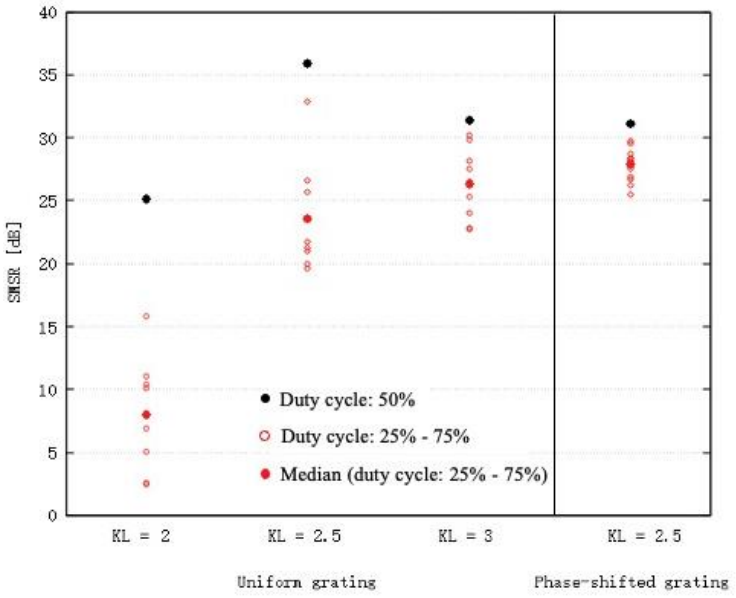

Figure 4.1 SMSR degradation of DFB lasers with the grating DCR under different normalized grating coupling coefficients

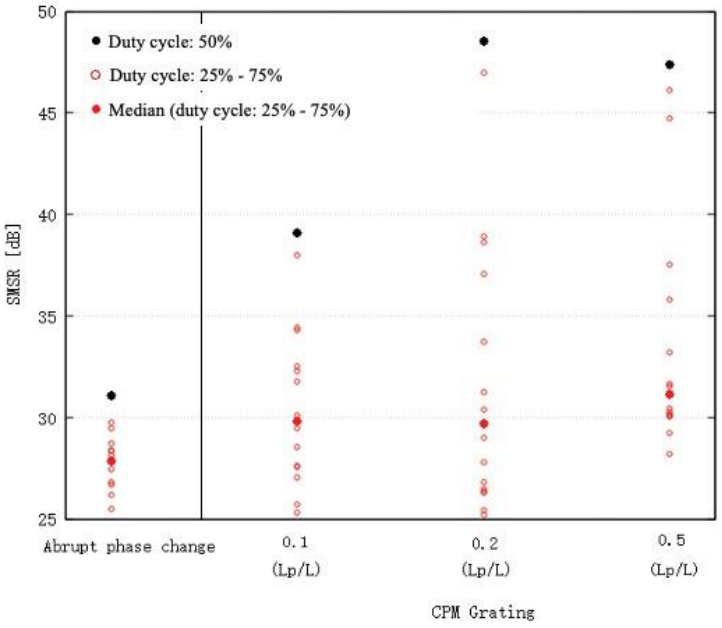

Figure 4.2 SMSR degradation of quarter-wavelength phase-shifted DFB lasers with their phase shifts made by abrupt change and CPM ($\kappa L = 2.5$)

It's well-known that the quarter-wavelength phase-shifted DFB laser provides a stable single mode operation with high SMSR, as it doesn't have the inherent dual mode degeneracy problem in uniform grating DFB lasers [31]. However, it suffers from the severe longitudinal spatial hole burning (LSHB) effect especially for high κL [32]. To mitigate the LSHB effect in quarter-wavelength phase-shifted DFB lasers, the corrugation pitch modulation (CPM) with the grating phase-shift distributed within a phase-arranging region (PAR) was proposed [33,34] to replace the conventional grating with an abrupt phase change. As shown in Fig. 4.2, in ideal case (black circular spots), the quarter-wavelength phase-shifted DFB laser with the CPM grating indeed has a much higher SMSR. With the grating DCR, however, its SMSR drops drastically. For DFB lasers with the CPM grating, their median values of SMSR have no significant advantage as compared to the

DFB laser with an abrupt phase-shifted grating, regardless of the CPM grating PAR length (L_p) ratio over the total cavity length (L). Moreover, the fluctuation of the SMSR for DFB lasers with the CPM grating is much higher than that for the DFB laser with the abrupt phase-shifted grating. This result reveals that the DCR has a stronger impact on the SMSR for CPM gratings. Namely, the CPM grating is advantageous to be adopted by the quarter-wavelength phase-shifted DFB lasers only if the grating DCR can be reduced to below certain extent. Otherwise, the effort to make CPM gratings for DFB lasers cannot be justified.

4.2 Effect of Grating DCR on Linewidth

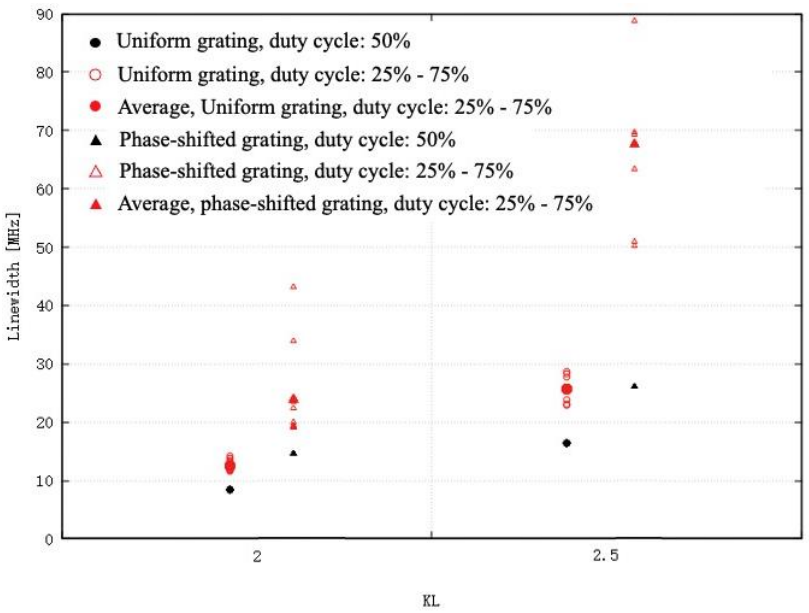

Figure 4.3 Linewidth broadening of DFB lasers with the grating DCR under different normalized grating coupling coefficients

Figure 4.3 shows the impact of the grating DCR on the linewidth of DFB lasers. As compared to the ideal grating without the DCR, while the linewidth is moderately broadened by ~40% for uniform grating DFB lasers with $\kappa L = 2$ ~2.5, it drastically increases by 1.6~2.5 folds for quarter-wavelength phase-shifted DFB lasers with κL falling in the same range. The fluctuation range of the linewidth for the quarter-wavelength phase-shifted DFB lasers is also substantially broader than that for the uniform grating DFB lasers.

The grating DCR brings in a significant linewidth broadening effect, with a greater impact on the quarter-wavelength phase-shifted DFB lasers as compared to the uniform grating DFB lasers with the same κL. There is also a trend that the linewidth broadening effect is more pronounced as κL increases, especially for the quarter-wavelength phase-shifted DFB lasers.

4.3 Effect of Grating DCR on RIN

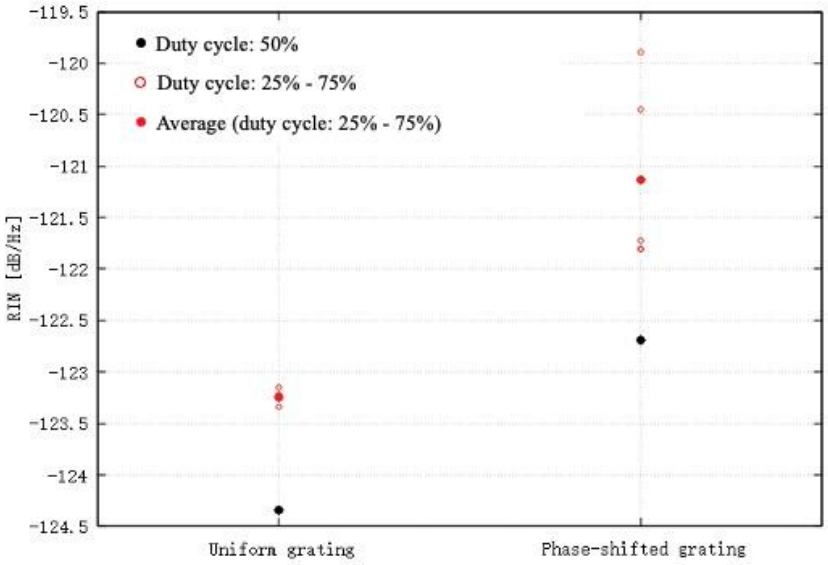

Figure 4.4 RIN of DFB lasers with the grating DCR under $\kappa L = 2.0$

Fig. 4.4 shows the effect of the grating DCR on the relative intensity noise (RIN) for DFB lasers with $\kappa L = 2.0$. As compared to the ideal grating without the DCR, the median RIN of the uniform grating and the quarter-wavelength phase-shifted DFB lasers with the grating DCR increases by 1.10 dB/Hz and 1.56 dB/Hz, respectively, with a fluctuation of RIN at 0.19 dB/Hz and 1.91 dB/Hz, respectively. This result indicates that the grating DCR only has a moderate impact on the RIN of either uniform grating or quarter-wavelength phase-shifted DFB lasers.

4.4 Effect of Grating DCR on Coupling Strength

Since the lasing spectrum can directly be obtained from the TMM approach [35,36], from which the Bragg stopband width can readily be found, we can therefore extract the effective grating coupling coefficient ($\bar{\kappa}$) [37] when the DCR exists.

Figs. 4.5 (a) and (b) present the calculated Bragg stopband widths of the uniform grating and the quarter-wavelength phase-shifted DFB lasers, respectively, with κL varying from 1.57 to 2.5. Shown on the left and right vertical axes are the Bragg stopband width and the corresponding effective grating coupling coefficient, respectively. With the grating DCR, an average reduction of ~20% on the grating coupling coefficient are found relative to the ideal grating coupling coefficient ($\bar{\kappa}/\kappa$), for either uniform grating or quarter-wavelength phase-shifted DFB lasers. Although the relative weakening to the grating coupling strength is the same for DFB lasers with different grating structures, the fluctuation of the effective grating coupling coefficient of the quarter-wavelength phase-shifted DFB lasers is more than doubled as compared to that of the uniform grating DFB lasers.

The grating DCR leads to an effective reduction on its coupling strength regardless of the grating structure and its coupling strength in ideal case (i.e., without the grating DCR), as evidenced by the shrinkage of its Bragg stopband width. This effect is attributed to the fact that the grating DCR jeopardizes the phase matching condition on the reflected and transmitted waves from pitch to pitch, thereby diminishing the coherence of the coupling between the contra-propagating waves.

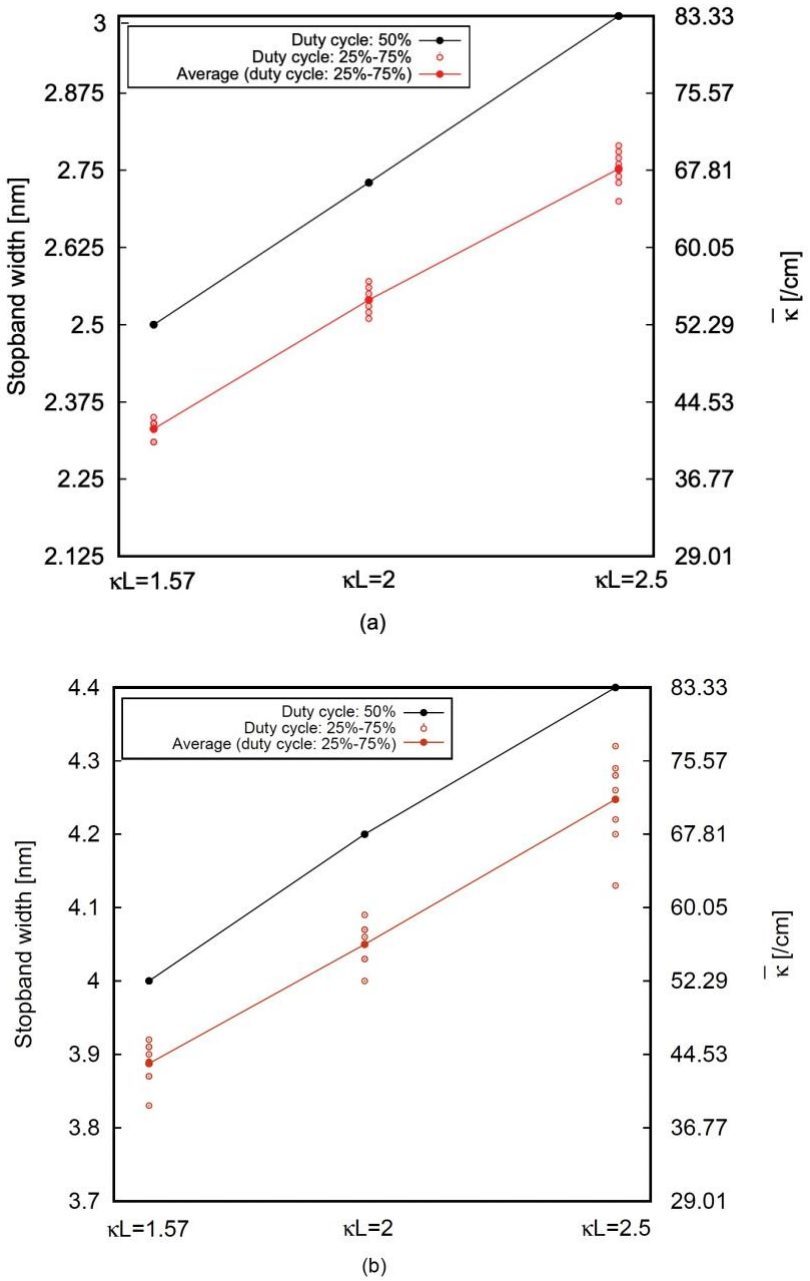

Figure 4.5 Bragg stopband width and effective grating coupling coefficient for (a) uniform grating DFB lasers, and (b) quarter-wavelength phase-shifted DFB lasers

The effective reduction on the grating coupling strength due the DCR should consequently reduce the LSHB effect. This is true as evidenced by the calculated photon and carrier

density distributions in DFB lasers with different grating structures as shown in Figs. 4.6 and 4.7.

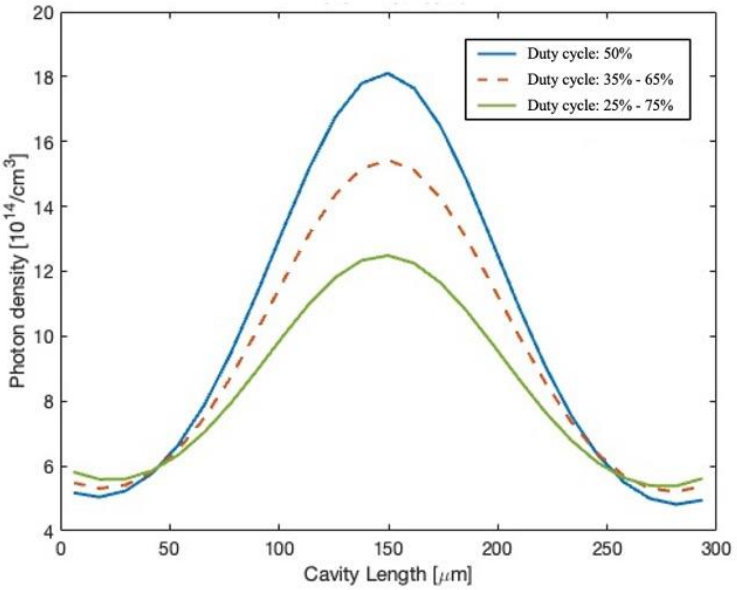

(a)

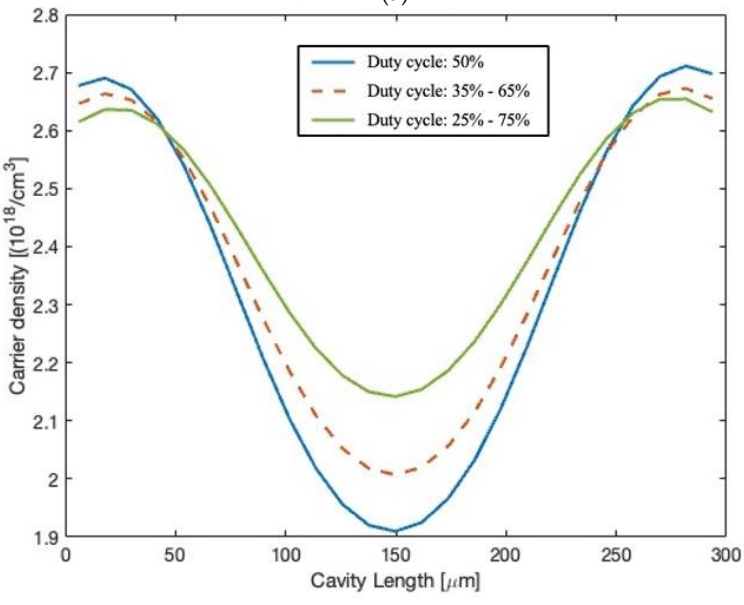

(b)

Figure 4.6 Photon (a) and carrier (b) density distributions of uniform grating DFB lasers with grating DCR at different levels ($\kappa L = 2.5$)

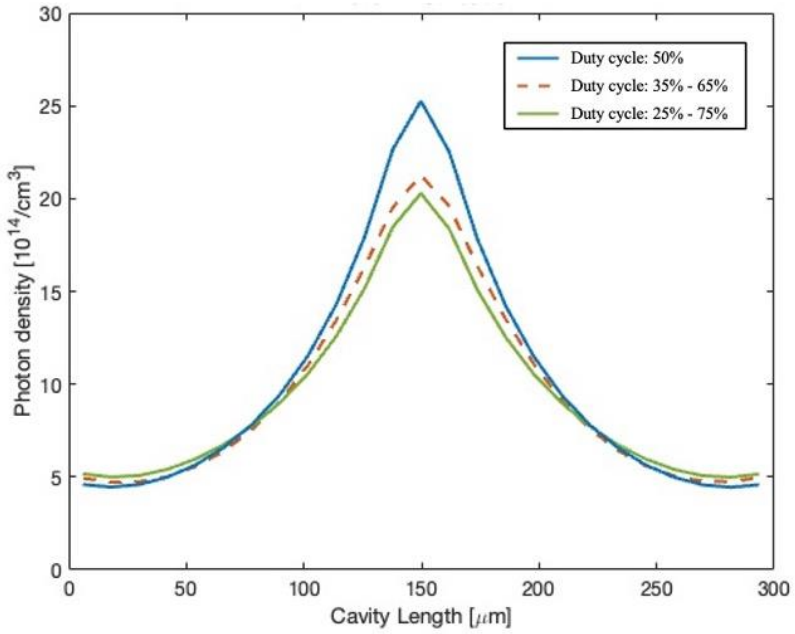

(a)

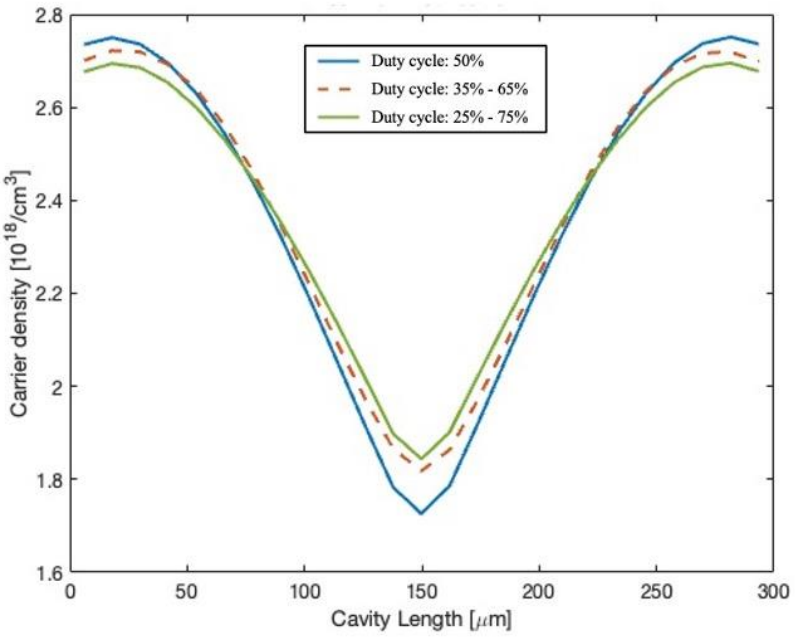

(b)

Figure 4.7 Photon (a) and carrier (b) density distributions of quarter-wavelength phase-shifted DFB lasers with grating DCR at different levels ($\kappa L = 2.5$)

Chapter 5

Conclusion

Based on a modified TMM approach that can handle the sub-period variation in Bragg grating, this thesis studied the impact of the grating DCR on DFB laser performance. The grating DCR effectively reduces the grating coupling strength, and consequently reduces the SMSR and broaden the linewidth. However, its effect on the RIN is moderate. The grating DCR brings a greater SMSR degradation to the uniform grating DFB lasers, whereas it gives a wider linewidth broadening to the quarter-wavelength phase-shifted DFB lasers. In general, the impact of the DCR is more pronounced as the grating coupling strength increases. Lastly, we find that the CPM grating can hardly be justified if the grating DCR cannot be diminished to some extent.

Bibliography

[1] Osanai, H., et al. "Effect of dopants on transmission loss of low-OH-content optical fibres." Electronics Letters 21.12 (1976): 549-550.

[2] Kao, K. Charles, and George A. Hockham. "Dielectric-fibre surface waveguides for optical frequencies." Proceedings of the Institution of Electrical Engineers. Vol. 113. No. 7. IET Digital Library, 1966.

[3] Alferov, Zh I., et al. "AlAs-GaAs heterojunction injection lasers with a low room-temperature threshold." Sov Phys Semiconductors 3.9 (1970): 1107-1110.

[4] Panish, M. B., I. Hayashi, and F. K. Reinhart. "Properties of double heterostructure injection lasers: Continuous room-temperature operation." 1970 International Electron Devices Meeting. IEEE, 1970.

[5] Shen, C. Co, J. Jo Hsieh, and T. A. Lind. "1500-h continuous cw operation of double-heterostructure GaInAsP/InP lasers." Applied Physics Letters 30.7 (1977): 353-354.

[6] Kogelnik, H., and C. Vo Shank. "Coupled-wave theory of distributed feedback lasers." Journal of applied physics 43.5 (1972): 2327-2335.

[7] Soda, Haruhisa, et al. "GaInAsP/InP surface emitting injection lasers." Japanese Journal of Applied Physics 18.12 (1979): 2329.

[8] Iga, Kenichi, Susumu Kinoshita, and Fumio Koyama. "Microcavity GalaAs/GaAs surface-emitting laser with Ith= 6 mA." Electronics letters 3.23 (1987): 134-136.

[9] Koyama, Fumio, Susumu Kinoshita, and Kenichi Iga. "Room-temperature continuous wave lasing characteristics of a GaAs vertical cavity surface-emitting laser." Applied physics letters 55.3 (1989): 221-222.

[10] Agrawal, Govind P., and Niloy K. Dutta. Semiconductor lasers. Springer Science & Business Media, 2013.

[11] Li, Xun. Optoelectronic devices: design, modeling, and simulation. Cambridge University Press, 2009.

[12] Tsang, C. F., et al. "Comparison between power matrix model and time domain model in modelling large signal responses of DFB lasers." IEE Proceedings-Optoelectronics 141.2 (1994): 89-96.

[13] Zhang, L. M., et al. "Dynamic analysis of radiation and side-mode suppression in a second-order DFB laser using time-domain large-signal traveling wave model." IEEE Journal of Quantum Electronics 30.6 (1994): 1389-1395.

[14] Kim, Byoung-Sung, Youngchul Chung, and Jae-Seung Lee. "An efficient split-step time-domain dynamic modeling of DFB/DBR laser diodes." IEEE journal of quantum electronics 36.7 (2000): 787-794.

[15] Tromborg, B., et al. "Traveling wave method for calculation of linewidth, frequency tuning, and stability of semiconductor lasers." IEEE Photonics technology letters 4.9 (1992): 985-988.

[16] Gioannini, Mariangela, and Mattia Rossetti. "Time-domain traveling wave model of quantum dot DFB lasers." IEEE Journal of Selected Topics in Quantum Electronics 17.5 (2011): 1318-1326.

[17] Li, W., et al. "Multiwavelength gain-coupled DFB laser cascade: design modeling and simulation." IEEE journal of quantum electronics 36.10 (2000): 1110-1116.

[18] Xi, Yanping, Xun Li, and Wei-Ping Huang. "Time-domain standing-wave approach based on cold cavity modes for simulation of DFB lasers." IEEE journal of quantum electronics 44.10 (2008): 931-937.

[19] Xi, Yanping, Wei-Ping Huang, and Xun Li. "An efficient solution to the standing-wave approach based on cold cavity modes for simulation of DFB lasers." Journal of lightwave technology 27.15 (2009): 3227-3234.

[20] Xi, Yanping, Wei-Ping Huang, and Xun Li. "A standing-wave model based on threshold hot-cavity modes for simulation of gain-coupled DFB lasers." Journal of lightwave technology 27.17 (2009): 3853-3860.

[21] Streifer, William, D. Scifres, and Robert Burnham. "Coupled wave analysis of DFB and DBR lasers." IEEE Journal of Quantum Electronics 13.4 (1977): 134-141.

[22] Kim, Byoung-Sung, Youngchul Chung, and Jae-Seung Lee. "An efficient split-step time-domain dynamic modeling of DFB/DBR laser diodes." IEEE journal of quantum electronics 36.7 (2000): 787-794.

[23] Hong, Jin, Weiping Huang, and Toshihiko Makino. "On the transfer matrix method for distributed-feedback waveguide devices." Journal of lightwave technology 10.12 (1992): 1860-1868.

[24] Yeh, P. "Optical Waves in Layered Media." (2006).

[25] Makino, T. "Transfer matrix method with applications to distributed feedback optical devices." Progress In Electromagnetics Research 10 (1995): 271-319.

[26] Osin Ski M, Polish M, Adams M J. Gain spectra of quaternary semiconductors[J]. IEE Proceedings I Solid State and Electron Devices. 1982, 129(6): 229.

[27] Zhao, S. Z. Numerical Simulation of a Combined Grating DFB Surface-Emitting Semiconductor Laser. 2013. Huazhong University of Science & Technology, Master's thesis

[28] Davis, M. G., and R. F. O'Dowd. "A new large-signal dynamic model for multielectrode DFB lasers based on the transfer matrix method." IEEE photonics technology letters 4.8 (1992): 838-840.

[29] Davis, M. G., and R. F. O'Dowd. "A transfer matrix method based large-signal dynamic model for multielectrode DFB lasers." IEEE Journal of Quantum Electronics 30.11 (1994): 2458-2466.

[30] Davis, M. G., and R. F. O'Dowd. "A transfer matrix-based analysis of multielectrode DFB lasers." IEEE Photonics technology letters 3.7 (1991): 603-605.

[31] Akiba, Shigeyuki, Masashi Usami, and Katsuyuki Utaka. "1.5-μm λ/4-shifted InGaAsP/InP DFB lasers." Journal of lightwave technology 5.11 (1987): 1564-1573.

[32] Li, Xun. "Longitudinal spatial hole burning, its impact on laser operation, and suppression." Science Bulletin 60 (2015): 1045-1046.

[33] Dai, Yitang, and Jianping Yao. "Numerical study of a DFB semiconductor laser and laser array with chirped structure based on the equivalent chirp technology." IEEE journal of quantum electronics 44.10 (2008): 938-945

[34] Okai, Makoto. "Spectral characteristics of distributed feedback semiconductor lasers and their improvements by corrugation-pitch-modulated structure." Journal of applied physics 75.1 (1994): 1-29

[35] Vankwikelberge, Patrick, Geert Morthier, and Roel Baets. "CLADISS-a longitudinal multimode model for the analysis of the static, dynamic, and stochastic behavior of diode lasers with distributed feedback." IEEE Journal of Quantum Electronics 26.10 (1990): 1728-1741.

[36] Tromborg, B. J. A. R. N. E., Henning Olesen, and Xing Pan. "Theory of linewidth for multielectrode laser diodes with spatially distributed noise sources." IEEE Journal of Quantum Electronics 27.2 (1991): 178-192.

[37] Okuda, H., et al. "Longitudinal-mode characteristics for 1.3 um GaInAsP/InP DFB lasers just below the threshold current." Electronics Letters 10.19 (1983): 362-363.